# MODELING OF NEAR INFRARED LASER-MEDIATED PLASMONIC HEATING WITH OPTICALLY TUNABLE GOLD NANOPARTICLES FOR THERMAL THERAPY

A Thesis
Presented to
The Academic Faculty

by

Francisco J. Reynoso

In Partial Fulfillment
of the Requirements for the Degree
Master of Science in the
George W. Woodruff School of Mechanical Engineering

Georgia Institute of Technology
December 2011

# MODELING OF NEAR INFRARED LASER-MEDIATED PLASMONIC HEATING WITH OPTICALLY TUNABLE GOLD NANOPARTICLES FOR THERMAL THERAPY

Approved by:

Dr. Sang Hyun Cho, Advisor
George W. Woodruff School of Mechanical
Engineering
*Georgia Institute of Technology*

Dr. C.-K. Chris Wang
George W. Woodruff School of Mechanical
Engineering
*Georgia Institute of Technology*

Dr. Eric Elder
Department of Radiation Oncology
*Emory University School of Medicine*


Date Approved: November 11, 2011

# ACKNOWLEDGEMENTS

I would like to thank my advisor, Dr. Sang Hyun Cho for giving me the opportunity to work with him. I feel extremely privileged to consider him my mentor. I am grateful to the other previous and current members of the lab for giving me the tools to make this work possible. I would also like to thank the rest of my committee, Dr. Eric Elder and Dr. Chris Wang for their time and invaluable suggestions. To my dear Sarah, thank you for your continuous words of encouragement and support. Finally, I would like to thank my mother for instilling in me the value of hard work and dedication.

# TABLE OF CONTENTS

# LIST OF TABLES

# LIST OF FIGURES

# SUMMARY

Clinical hyperthermia refers to treatment of tumors by heating the lesions between 40 and 45° C. Several clinical trials have demonstrated that hyperthermia provides significant improvements in clinical outcomes for a variety of tumors, especially when combined with radiotherapy. However, its routine clinical application is still not optimal and major improvements are needed. The temperature distributions achieved are far from satisfactory and improved temperature control and monitoring are still in need of further development. The use of gold nanoparticles (GNPs) has emerged as a good method to achieve local heat delivery when combined with near-infrared (NIR) laser. GNPs have a plasmon resonance frequency that can be tuned to absorb strongly in the NIR region where tissue absorption of laser light is minimal, allowing for less tissue heating and better penetration. For further development of the technique and appropriate clinical translation, it is essential to have a computational method by which the temperature distribution within the tumor and surrounding tissue can be estimated. Previously, our group developed a technique to estimate the temperature increase in a GNP-filled medium, by taking into account the heat generated from individual GNPs. This method involved a two-step approach combining the temperature rise due to GNPs and the solution to the heat equation using the laser light as heat source. The goal of this project was to develop a one-step approach that calculates the temperature distribution using the solution to the heat equation with multiple heat source terms, the laser light, and each individual GNP. This new method can be of great use in developing a treatment planning technique for GNP-mediated thermal therapy including hyperthermia.

# CHAPTER I

## INTRODUCTION

Hyperthermia is a therapeutic procedure in which tissues are exposed to elevated temperatures with the goal of locally treating a disease. Reports of hyperthermia treatments have existed as early as 3000 BC in the Egyptian Edwin Smith papyrus [18]. In 1898, the Swedish gynecologist Westermark published a paper describing the large regression of large carcinomas of the uterine cervix after local hyperthermia [8]. A worldwide interest in hyperthermia was sparked during the first international congress on hyperthermic oncology in Washington in 1975. Initial interest was evident with an exponential increase in publications related to the topic. However, interest faded due to unfavorable clinical results and reluctance among sponsoring authorities to support further research. In recent years, interest has been renewed due to improved treatment techniques and more favorable experimental results [18]. Laser-induced thermal therapy (LITT) is one of the leading treatment modalities currently under investigation.

It has long been known that the power of light plays an important role in multiple biological processes, but overexposure can have serious complications. Complete control of light exposure is the key to using the power of light for human benefit. Laser light can be very well controlled and therefore has found a multitude of medical applications. There are multiple ways that laser light can interact with tissues and each finds a different use in medicine. These effects are used in a variety of medical procedures that range from tissue cutting and welding in surgical procedures, to photodynamic therapy in oncology to destroy cancerous tumors [4]. Among all uses, laser use in surgery is the most significant and has become an irreplaceable tool of modern medicine [15].

Laser use in thermal therapy has long held great promise, but has never been carried out with great success. Tissue penetration, inability to selectively heat the target, and a lack of predictive heat control have prevented its widespread clinical use. Recently, gold nanoparticles (GNPs) have been proposed to enhance the treatment efficacy of LITT. This

type of nanoparticle has a plasmon resonance that can be easily tuned to absorb strongly in the near-infrared (NIR) region. The present research aims to formulate a computational model that will predict local heating from individual GNPs in tissue. A method of this type would allow for the prediction of local heat distributions for any arbitrary distribution of GNPs at their target site. Particularly it aims towards development of a method that requires only the absorption and scattering properties of the tissue and GNPs separately, not of a GNP-filled region as a new type of interacting medium. The absorption and scattering properties of tissue and GNPs can be measured independently and the distribution of GNPs can be deduced from imaging studies. This approach would be preferred over attempting to measure the absorption and scattering properties of a tissue-like medium filled with an unrealistic homogeneous GNP distribution.

Previously, our group developed a technique to estimate the temperature increase in a GNP-filled medium, by taking into account the heat generated from individual GNPs. This method involved a two-step approach combining the temperature rise due to nanoparticles and the solution to the heat equation using the laser light as heat source. The goal of the current project was to develop a one-step approach that calculates the temperature distribution using the solution to the heat equation with multiple heat source terms, the laser light, and each individual GNP. The new method can be of great use in developing a treatment planning technique for GNP-mediated thermal therapy including hyperthermia.

# CHAPTER II

# BACKGROUND

## 2.1  Interactions between Light and Tissue

### 2.1.1  Effects of biological tissue on light absorption and scattering

It is well understood that when light impinges on matter, three main effects are observed: reflection and refraction, absorption, and scattering. The only photons that are transmitted are those that are not reflected or absorbed, and those that are forward-scattered. The fraction of photons that undergo each interaction is mainly dependent on the type of material and the wavelength of light. In opaque matter like tissue, reflection and refraction are difficult to measure, and absorption and scattering are the dominant types of interactions [15].

When electrons in matter are exposed to light, they are set in motion by the electric field. If the frequency of light matches the natural frequency of oscillation of the particles, they absorb significant energy. Therefore, the intensity of the incident light field is attenuated as it passes through the medium, depositing energy throughout. The amount of light that is absorbed by the medium is described by the absorption coefficient $\mu_a (cm^{-1})$ defined in Beer-Lambert's law, and only takes into account photon losses due to absorption. The predominant chromophores in vascularized tissue are melanin and hemoglobin, both of which show decreased absorption in the infrared region between 600 nm and 1200 nm. This range of wavelengths represent the 'therapeutic window' of laser light [15].

Scattering occurs when light interacts with electrons, but the frequency does not match the natural frequency of the particle's oscillation. The particles are forced into motion, and while the vibration will have the same frequency and direction as that of the electric field of light, the magnitude is far smaller than that of absorption. The phase of oscillation is different than that of the incident light, causing photons to slow down and scatter into different directions. This results in loss of intensity of the primary photons and described by the scattering coefficient $\mu_s (cm^{-1})$ defined with Beer-Lambert's law but taking into account

photon losses solely due to scattering. Photons in biological tissues are predominantly scattered in the forward direction. This behavior is characterized using an anisotropy coefficient $g$ defined using the probability function $p(\theta)$ of a photon being scattered by an angle $\theta$ using:

$$g = \frac{\int_{4\pi} p(\theta) cos(\theta) d\Omega}{\int_{4\pi} p(\theta) d\Omega} \tag{1}$$

where $d\Omega = sin(\theta)d\theta d\varphi$ is the differential solid angle. This means that $g = 1$ represents pure forward scattering and $g = -1$ represent pure backscattering. The values of $g$ for most biological tissues range from 0.7 to 1. The anisotropy factor is useful in defining a reduced scattering coefficient $\mu'_s = \mu_s(1 - g)$ which accounts for the fraction of scattering events that are not forward-directed [15]. Table 1 shows a list of all optical parameters needed to characterize the behavior of light through a medium.

**Table 1:** Optical Parameters

| | |
|---|---|
| Absorption Coefficient | $\mu_a$ $(1/m)$ |
| Scattering Coefficient | $\mu_s$ $(1/m)$ |
| Anisotropy Factor | $g$ |
| Reduced Scattering Coefficient | $\mu'_s$ $(1/m)$ |

### 2.1.2 Effects of light on biological tissue

There are a multitude of effects on matter that can occur when laser light is applied to biological tissues. The type of effects that actually occur are not only heavily dependent on tissue properties but also on various laser parameters: power, focal spot size, wavelength, and exposure time. These effects are categorized into: photoablation, photodisruption, photochemical interactions, plasma-induced ablation, and thermal interactions. All of these effects have a variety of uses in medicine, but thermal interactions are the only effects of interest for LITT. Surprisingly, selecting the appropriate parameters to produce the desired interaction type is mainly dependent on the exposure time. All these interaction types occur with energy densities that range from 1 $J/cm^2$ to 1000 $J/cm^2$, but by adjusting exposure times, power densities can differ by $\sim$ 15 orders of magnitude. Figure 1 shows a log-log plot that displays the power density and exposure times needed to produce a variety of interaction types. The exposure times that are considered for LITT are on the
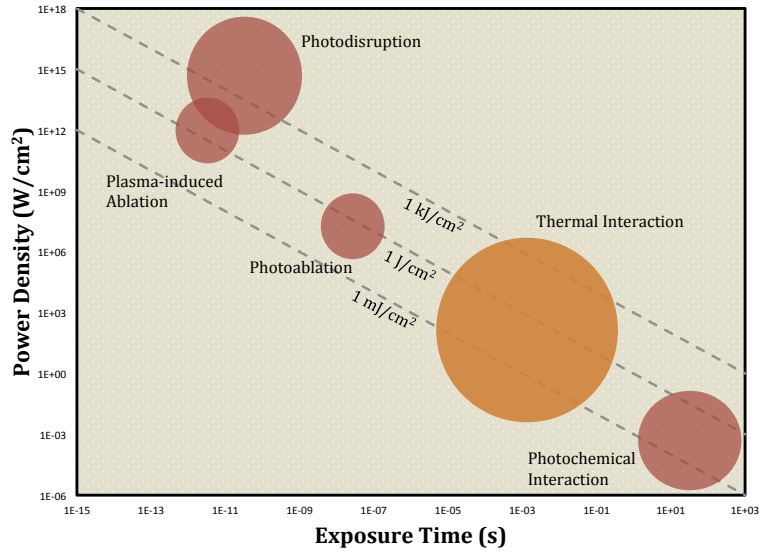
**Figure 1:** Laser-tissue interactions and associated laser parameters at which they dominate. Figure redrawn from [15].

order of seconds with power densities on the order of $10^4$ $W/cm^2$ which fall in the thermal interaction regime [15].

## 2.2 Photo-thermal Effects

Photo-thermal effects are one of the first laser-tissue interactions to be studied, as it does not require short laser pulses, which were not always available [14]. Photo-thermal effects are unique among other effects as there is no specific reaction pathway required to achieve damage; heat can be absorbed by any biomolecule and lead to tissue damage. Photo-thermal effects are also unique in the sense that tissue damage is only dependent on the temperature that is reached and the duration at which it remains at that temperature [4, 14]. This means that in order to characterize and correctly predict tissue damage from thermal therapy, only the spatial and temporal distribution of heat is needed. This can be obtained in three main steps: determine the optical and thermal parameters of the tissue, determine photon absorption from transport theory, and solve the heat diffusion equation (Figure 2).

In order to observe the macroscopic effect that is an increase in temperature, the photo-thermal process starts with the absorption of energy from a photon and its subsequent

5
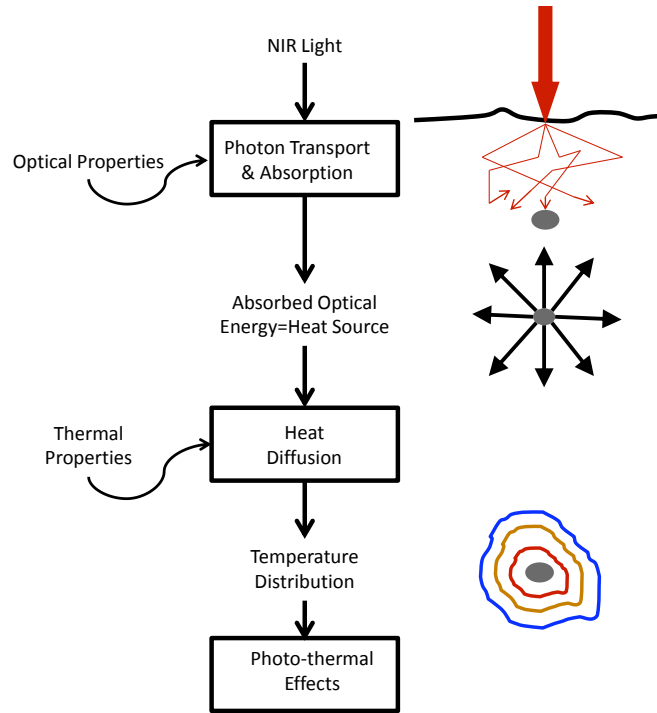
**Figure 2:** Process flow needed to predict tissue damage from LITT. Figure redrawn from [4].

conversion into heat energy via molecular vibrations and collisions. The absorption of a photon by a molecule hinges on the availability of accessible vibrational states which are numerous for most biomolecules. This makes the absorption process highly efficient in biological tissues [1].

The thermalization process in biological tissue is a non-radiative, de-excitation pathway that occurs when a molecule absorbs a photon and during its excited state collides with other molecules. The vibrational energy in the excited molecule is transferred to other molecules as translational kinetic energy, which macroscopically manifests itself as a temperature increase. This process is referred to as thermal relaxation and while this process occurs on the order of picoseconds, a macroscopic increase in temperature is only evident on a much larger timescale on the order of seconds [11].

In this project, only continuous laser illumination was considered, and heat deposition due to continuous laser exposure was a direct function of the energy flux density or light fluence rate $\varphi(\vec{r}, t)(W/m^2)$ and the absorption coefficient $\mu_a(m^{-1})$. The absorbed power

density $Q(\vec{r}, t)$ is:

$$Q(\vec{r}, t) = \mu_a \varphi(\vec{r}, t) \tag{2}$$

The term $Q(\vec{r}, t)$ is then the amount of optical energy being deposited as heat at $\vec{r}$ at time $t$. This means that maximum heat deposition occurs when the product of the absorption coefficient and light fluence is a maximum.

It is clear that in order to achieve efficient heating at a disease site such as a cancerous tumor, deep light penetration with an increase in absorption coefficient at the target site is needed. The use of GNPs has emerged as a good method to achieve local heat delivery during LITT. GNPs have a plasmon resonance frequency that can be tuned to absorb strongly in the NIR region where tissue absorption is minimal, allowing for less tissue heating and better penetration. The increased absorption properties of these GNPs compared to the surrounding tissue results in preferential heating of GNPs. The GNPs can be delivered into solid tumors and subsequently illuminated with NIR laser light, achieving highly conformal heat delivery to the tumor site [3, 6].

## 2.3  Surface Plasmon Resonance

The interesting optical properties of noble metal nanoparticles have been unknowingly in use for hundreds of years. Their bright and intense colors can be seen in stained cathedral windows and other forms of artwork for centuries [11, 5, 12]. The physicist Michael Faraday was the first to show that the properties of these intense dyes was due to colloidal Au present in the solution [5]. In 1908, Gustav Mie presented the first solution to Maxwell's equations that describes the extinction spectra due to scattering and absorption of spherical nanoparticles of any size [12, 11].

The physical basis for this phenomenon is called surface plasmon resonance (SPR). The illumination of a small metallic nanoparticle by light causes the conduction electrons to respond to the electric field of the incident light. These electrons are collectively displaced, and as a result of the Coulomb attraction from the nucleus, the electron cloud collectively oscillates (Figure 3). The frequency of oscillation is dependent on four factors: the effective electron mass, the density of electrons, and the size and shape of the charge distribution
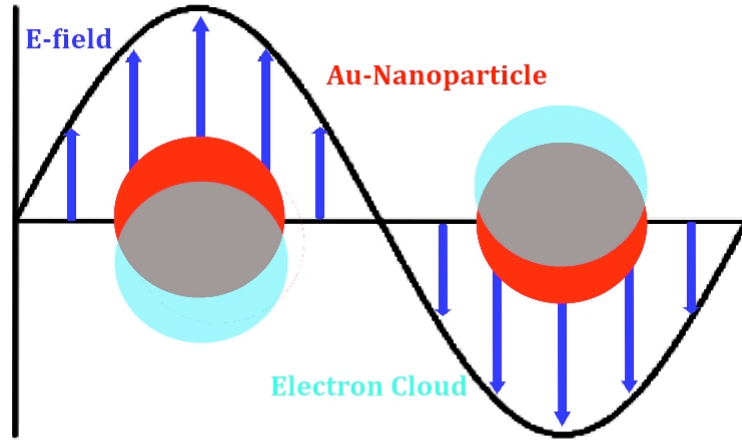
**Figure 3:** Electron cloud oscillations for a spherical nanoparticle. Figure redrawn from [12].

[12]. It can be shown that for small particles with a size much smaller than the wavelength of light, only the dipole mode of oscillation dominates with a polarizability $\alpha$ given by [11]:

$$\alpha = 3\epsilon_o V \frac{\epsilon - \epsilon_m}{\epsilon + 2\epsilon_m} \tag{3}$$

where $V$ is the particle volume, $\epsilon_o$ is the vacuum permittivity, $\epsilon$ is the complex frequency-dependent dielectric function of the metal, and $\epsilon_m$ is the dielectric constant of the surrounding medium. The polarizability shows a strong resonance peak for values of $\epsilon = -2\epsilon_m$, which defines the SPR frequency [11]. The SPR frequency depends not only on the type of metal but also on the size and shape of the nanoparticles. This allows for the tuning of the SPR frequency to a wide range of frequencies in the NIR and UV range. It is also evident that for anisotropic nanoparticles like nanorods, two SPR modes exist, a longitudinal mode and a transverse mode, that allow for improved tunability.

The unique optical properties of noble metal nanoparticles have made them a unique tool in biological imaging and therapeutics [11]. The attractive feature of this class of nanoparticles for LITT is the efficient conversion of absorbed energy to heat. The plasmon absorption process is a non-radiative process that converts the absorbed energy to heat via electron-electron and electron-phonon relaxations on the order of picoseconds. This

efficient heating mechanism overcomes the failure of other LITT to selectively heat tumor regions. GNPs can be selectively accumulated within a tumor via the enhanced permeability and retention (EPR) effect [13], and target molecules to produce highly conformal heat distribution when used in conjunction with LITT.

## 2.4 Radiative Transport Theory

In order to determine the light distribution within a medium, radiative transport theory may be applied [10]. An approximation can be made when scattering processes dominate absorption processes, as is the case in biological tissue ($\mu_a << \mu_s$). This is referred to as the light diffusion approximation and described by:

$$-D\nabla^2\varphi(\vec{r}) + \mu_a\varphi(\vec{r}) = s(\vec{r}) \tag{4}$$

where $\varphi(\vec{r})$ ($W/m^2$) is the light fluence rate, $s(\vec{r})$ ($W/m^3$) is the light source term, and D (m) is the diffusion coefficient defined as:

$$D = \frac{1}{3(\mu_s' + \mu_a)} \tag{5}$$

where $\mu_s' = (1-g)\mu_s$ is the reduced scattering coefficient as defined in section 1.2.1. The diffusion approximation is appropriate and studies [9, 15] have shown values of $\mu_s$ are two to three orders of magnitude larger than $\mu_a$ for biological tissues and NIR light. More importantly, the approximation should hold true for water and water-based gel phantoms. While there are no published results for such phantoms, it is safe to assume the optical properties of gel phantoms approximate those of water as they are mostly water-based (i.e. 98.5 wt. %) [3]. The solution to the light diffusion approximation for a continuous wave laser beam at the origin is given by:

$$\varphi(\vec{r},t) = \frac{P_o exp(-\mu_{eff}\vec{r}\cdot\hat{n})}{4\pi Dr} \tag{6}$$

where $\mu_{eff} = \sqrt{3\mu_a(\mu_a + \mu_s')}$ is the effective attenuation coefficient, $\hat{n}$ is the direction of beam travel, and $P_o$ is the laser power.

9

## 2.5  Heat Diffusion Equation

The heat distribution within the tissue is determined by the inhomogeneous heat equation:

$$\rho C \frac{\partial T(\vec{r}, t)}{\partial t} = \nabla \cdot [\kappa \nabla T(\vec{r}, t)] + Q \tag{7}$$

where $\rho$ $(kg/m^3)$ is the density, $C$ $(J/kg\,K)$ is the specific heat, $\kappa$ $(W/m\,K)$ is the thermal conductivity of the medium, and $Q$ $(W/m^3)$ is the heat source term. At the boundaries, heat transfer can be modeled via Neumann boundary condition:

$$-\kappa \frac{\partial T(\vec{r}, t)}{\partial n} = h(T_b - T_\infty) \tag{8}$$

where $h$ is the heat convection constant, $T_b$ is the temperature at the boundary, and $T_\infty$ is the ambient temperature. Table 2 shows a list of all thermal parameters needed to characterize heat diffusion through the medium.

The model presented here takes into account the heat generated from individual GNPs and the laser source separately. This is modeled in the heat diffusion equation by using multiple heat sources, a laser heat source, and one independent heat source for each individual nanoparticle:

$$Q = Q_{laser} + Q_{NP}$$
$$= Q_{laser} + \sum_{i=1}^{N} Q_i$$

where $Q_{laser}$ is the heat source due to laser light alone, $Q_{NP}$ is the heat source due to the ensemble of GNPs, $Q_i$ is the heat source due to an individual GNP, and $N$ is the total number of GNPs.

The heat generated due to laser light at $\vec{r}$ at time $t$ is denoted by:

$$Q_{laser}(\vec{r}, t) = \mu_a \varphi(\vec{r}, t) \tag{9}$$

where $\mu_a$ is the tissue absorption coefficient and $\varphi(\vec{r}, t)$ is the laser light fluence rate as described in section 1.3. The heat generated by the $ith$ nanoparticle at position $\vec{r_i}$ at time t is described by

$$Q_i(\vec{r}, t) = \sigma_a \varphi(\vec{r}, t) \delta(\vec{r} - \vec{r_i}) \tag{10}$$

10

where $\sigma_a$ is the absorption cross section of the gold nanoparticles and $\delta(\vec{r} - \vec{r_i})$ is the dirac delta function. The dirac delta function is used to describe the spatial distribution of the heat generated by each nanoparticle.

**Table 2:** Thermal Parameters

| Density | $\rho \ (kg/m^3)$ |
|---|---|
| Specific Heat | $C \ (J/kg\,K)$ |
| Thermal Conductivity | $\kappa \ (W/m\,K)$ |
| Convection Constant | $h \ (W/m^2\,K)$ |

# CHAPTER III

# LINEAR SUPERPOSITION MODEL

## 3.1  Theory

There is no analytical solution to the heat diffusion equation presented in the previous chapter. Recently, our research group proposed a multi-step method that calculates the rise in temperature due to individual GNPs and superimposes them to obtain the full heat distribution [3]. This method is valid as a direct result that the heat diffusion equation of this form is a linear differential equation:

$$\rho C \frac{\partial T(\vec{r}, t)}{\partial t} = \nabla \cdot [\kappa \nabla T(\vec{r}, t)] + Q$$

$$\Downarrow$$

$$\rho C \frac{\partial T_{laser}(\vec{r}, t)}{\partial t} = \nabla \cdot [\kappa \nabla T_{laser}(\vec{r}, t)] + Q_{laser}$$

$$+$$

$$\sum_{i}^{N} \rho C \frac{\partial T_i(\vec{r}, t)}{\partial t} = \sum_{i}^{N} \nabla \cdot [\kappa \nabla T_i(\vec{r}, t)] + \sum_{i}^{N} Q_i$$

The time independent temperature rise at point $\vec{r}$, due to constant NIR illumination of a single GNP at $\vec{r_i}$ in a homogeneous medium, is derived from the equation of heat conduction as presented in Carslaw and Jaeger [2] and given by:

$$\Delta T_i(\vec{r}) = \frac{\sigma_a \varphi(\vec{r})}{4\pi\kappa|\vec{r} - \vec{r_i}|} \tag{11}$$

The time dependent temperature rise in a homogeneous medium with no perfusion can be obtained using a Green's function and equation (10) as shown on a model presented in [16]:

$$\Delta T_i(\vec{r}, t) = erfc\left(|\vec{r} - \vec{r_i}|\sqrt{\frac{C\rho}{4\kappa t}}\right) \frac{\sigma_a \varphi(\vec{r})}{4\pi\kappa|\vec{r} - \vec{r_i}|} \quad for\ t \leq t_o \tag{12}$$

where $t_o$ is the time at which the laser is turned off. When the laser is turned off at $t = t_o$ the heat equation becomes homogeneous and the solution is simply:

$$\Delta T_i(\vec{r}, t) = \Delta T_{oi} exp\left(-\frac{t}{\tau}\right) \quad for\ t > t_o \tag{13}$$

where $\Delta T_{oi}$ is the temperature rise at $t = t_o$ and $\tau$ is the "thermal diffusion time constant" of the medium.

The temperature increase due to the laser alone, $\Delta T_{laser}(\vec{r}, t)$ can be obtained using a commercial finite element method (FEM) package (COMSOL Multiphysics 4.1, Comsol, Inc. , Burlington, MA.). The method is therefore a simple superposition of the solution of the heat equation due to each individual heat source, and referred to as the linear superposition method. The total change in temperature at $\vec{r}$ at time $t$ is therefore:

$$\Delta T(\vec{r}, t) = \Delta T_{laser} + \Delta T_N \tag{14}$$

$$\Delta T_N = \sum_{i=1}^{N} \Delta T_i \tag{15}$$

## 3.2 Phantom Experiment

The model used to test out the computational methods developed was based on a phantom experiment performed in our lab. The phantom was a breast phantom as shown in Figure 4 made of 1.5 wt. % agar gel. The long axis diameter of the phantom was 12 cm and the short axis diameter was 5 cm. A spherical cavity with a radius of 2 mm was inserted as shown in Figure 4. The cavity was filled with 0.1 wt. % gold nanorod (GNR) solution. The dimensions of each GNR are 12 nm in diameter and 40 nm in height, and an absorption cross section of $\sigma_a = 5.474 \times 10^{-15}\ m^2$ [11]. The total number of GNRs in the cavity was calculated as $N = 3.26 \times 10^{11}$, noting approximately 85% of the cavity volume was filled with the GNR solution. A 1.0 W 808 nm laser was applied to the phantom as shown in Figure 4.

**Table 3:** Phantom Properties

| | |
|---|---|
| Absorption Coefficient | $\mu_a = 2.2\ (1/m)$ |
| Anisotropy Factor | $g = 0.9$ |
| Density | $\rho = 1000\ (kg/m^3)$ |
| Thermal Conductivity | $\kappa = 0.587[1 + 0.0028(T - 20)]\ (W/kg\,K)$ |
| Specific Heat | $C = 3900\ (J/kg\,K)$ |
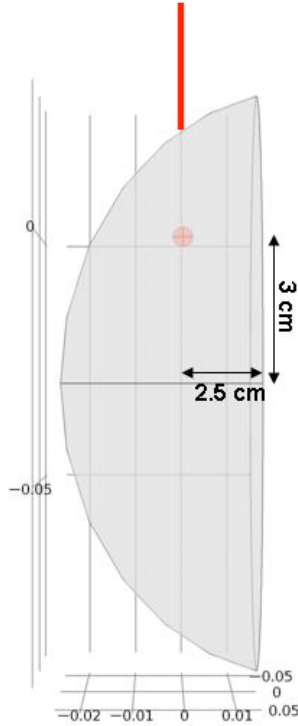
**Figure 4:** Breast phantom model made of 1.5 wt. % agar gel.

The optical parameters for the 1.5 wt. % agar gel used are not clearly known. However, they are expected to be very close to those of water and comparable to those of biological tissue. The optical parameters used were based on literature research [9, 15] and the measurements obtained during the experiment. The physical parameters chosen are shown on Table 3 and $\mu_s$ was allowed to be a free parameter in order to match experimental results. The experimental results showed an increase in temperature of about 15°C within the cavity after 60 seconds of NIR illumination. This was assumed to be the maximum temperature within the cavity. This assumption is not necessarily valid, but for the purpose of comparison between the two computational models is also not important.

### 3.3 Results

The linear superposition method was applied to the phantom described in section 2.2 using a MATLAB algorithm that calculated the temperature rise from each GNP at position $\vec{r}$ and time $t$, and combined the results with the laser component from FEM. The position of each GNP within the cavity was randomly generated. In order to reduce computation
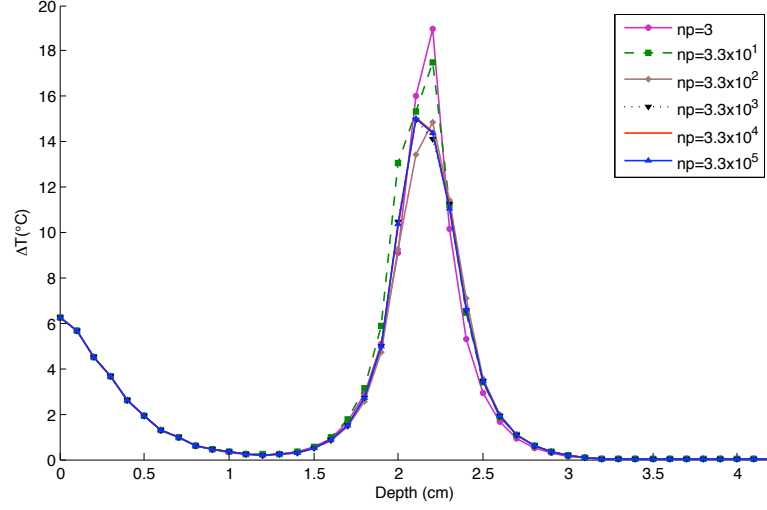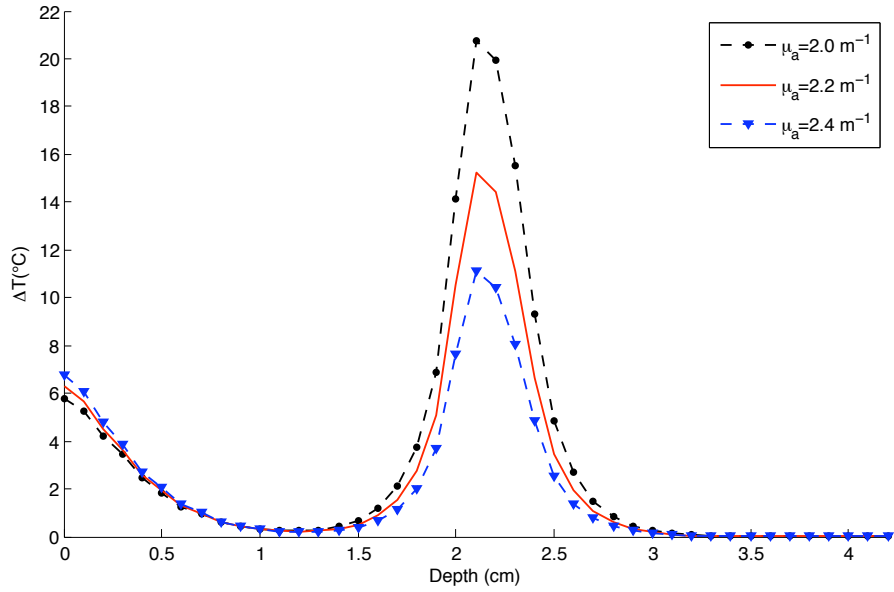
**Figure 5:** Temperature Profile at t=1 min along the laser axis on the breast phantom. Curves are shown for different values of reduced number of nanoparticles $np$.

time, the number of GNP was minimized and a corrective multiplication factor was used:

$$\Delta T_N = M \left( \sum_{i=1}^{np} \Delta T_i \right) \tag{16}$$

where $M = N/np$ is the multiplication factor, and $np$ is the reduced number of GNPs. Figure 5 shows the temperature increase profile down the central axis of the laser and shows convergence to less than 0.5% for $np \geq 10^4$.

The values of $\mu_a$ and $\mu_s$ were also varied to demonstrate appropriate behavior of the temperature distribution. As shown in Figure 6, a larger value of $\mu_a$ results in increased surface heating and less tissue penetration. This means decreased heating within the cavity as the beam is more heavily attenuated. Conversely, a smaller value of $\mu_a$ yields reduced surface heating and increased heating within the cavity. Similar conclusions can be drawn from Figure 7 where the scattering coefficient is changed. Finally, a 2D map of the temperature distribution within the phantom is shown in Figure 8. The results led to the choice of $\mu_s' = 16000m^{-1}$ for a maximum temperature rise of $15°$ C within the cavity. This maximum temperature was achieved approximately 7 mm above the center of the cavity, closer to the laser source.

15

**Figure 6:** Temperature Profile at t=1 min along the laser axis on the breast phantom. Curves are shown for different values of absorption coefficient $\mu_a$.
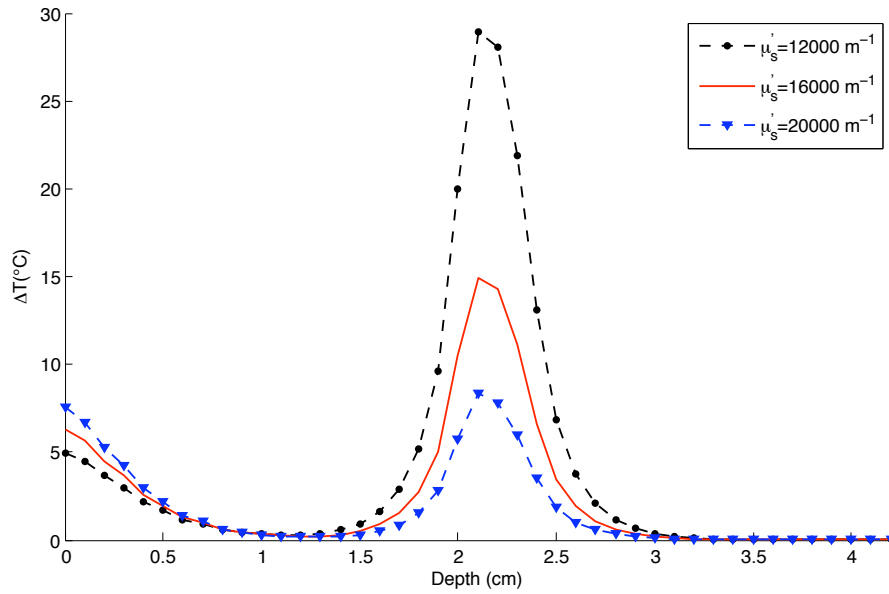


**Figure 7:** Temperature Profile at t=1 min along the laser axis on the breast phantom. Curves are shown for different values of reduced scattering coefficient $\mu'_s$.

16
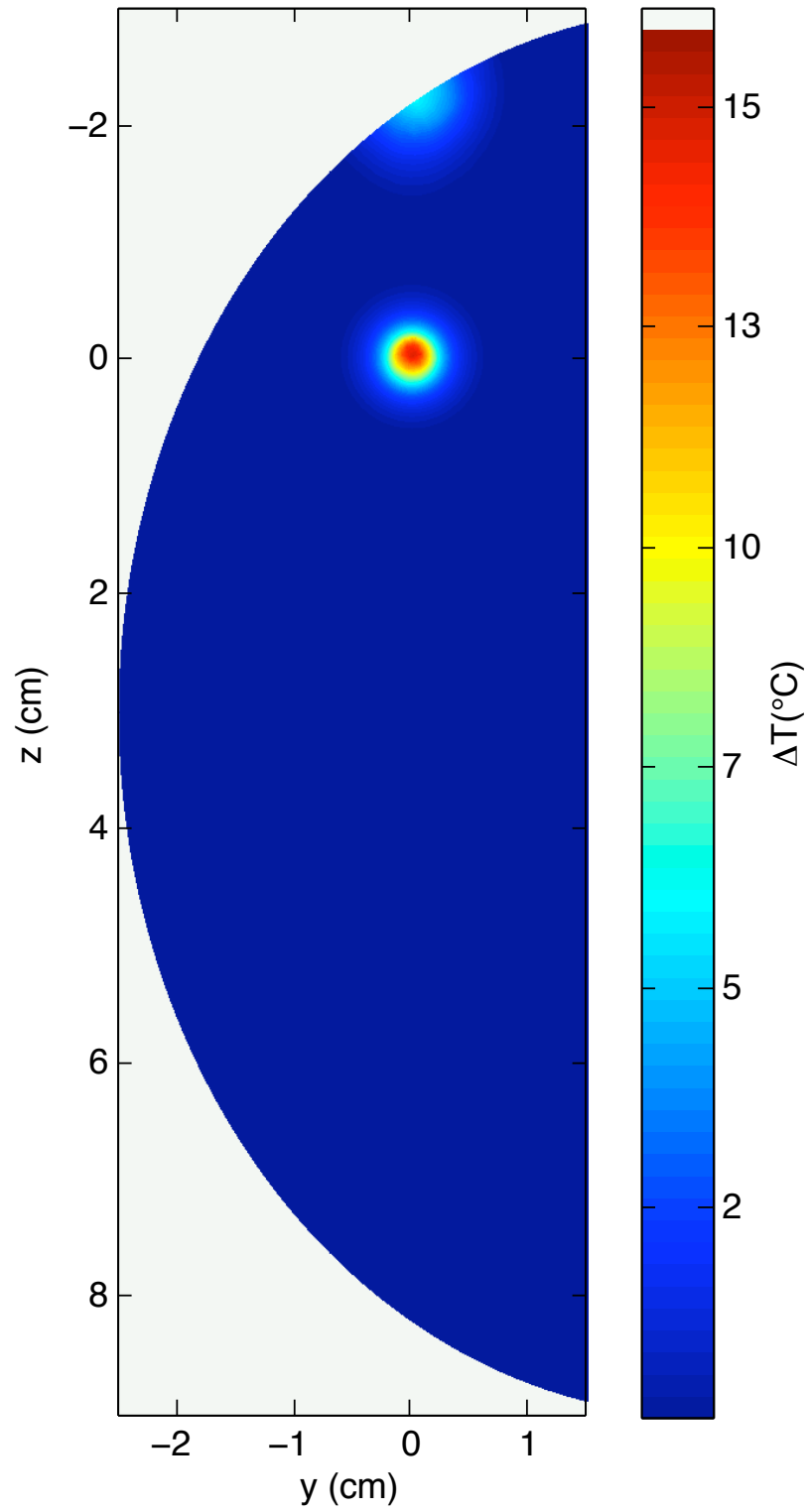
**Figure 8:** 2D Temperature Distribution at t=1 min within breast phantom using the Linear Superposition Method.

# CHAPTER IV

# FINITE ELEMENT METHOD

## *4.1 Theory*

The premise of solving a problem using the finite element method (FEM) is to find the solution of a complex problem by replacing it with a simpler problem. The solution to this simpler problem is not the *exact* solution of the problem but in many cases this is the only available solution. Furthermore, the approximate solution can be improved with more computational power. In the FEM, the solution region to a differential equation is considered to be built of multiple small interconnected regions called finite elements. A solution is approximated in each element, with the constraint that all solutions match at the boundary. This process is equivalent to replacing the differential equation with a set of expressions [17].

The heat diffusion equation as presented in equation (7) is referred to as the strong form of a problem as it requires strong continuity of all associated variables. This means that all variables need to be differentiable up to the order of the differential equation. This is usually very difficult to find, and the equation must be rewritten in the weak form. The weak form of a differential equation is an integral form of the original equation with much weaker requirements on the continuity of all associated variables. The weak form of the differential equation is the basis for constructing a finite element solution [17].

The weak form of a differential equation can be constructed following these steps:

1) Multiply the differential equation by an arbitrary test function.

2) Integrate the new equation over the whole domain.

3) Integrate by parts using Green's theorem to reduce derivatives to a lower order.

4) Replace boundary conditions for the new form of the differential equation.

Using this method, it can be shown that the weak form of the heat equation is:

$$\rho C \int_V u \frac{\partial T'(\vec{r},t)}{\partial t} dV = \int_V u \nabla \cdot [\kappa \nabla T'(\vec{r},t)] dV + \int_V u(Q_{laser} + Q_{NP}) dV$$

where $T'(\vec{r},t)$ is the weak form solution, and $u$ is an arbitrary test function that is continuously differentiable. Integrating by parts it becomes:

$$\rho C \int_V u \frac{\partial T'(\vec{r},t)}{\partial t} dV = \int_V \nabla \cdot [u\kappa \nabla T'(\vec{r},t)] dV$$

$$- \int_V \kappa \nabla u \cdot \nabla T'(\vec{r},t) dV + \int_V u(Q_{laser} + Q_{NP}) dV$$

and applying Green's Theorem on the first term of the RHS the equation becomes:

$$\rho C \int_V u \frac{\partial T'(\vec{r},t)}{\partial t} dV = \int_A u\kappa \nabla T'(\vec{r},t) \cdot \hat{n} dA$$

$$- \int_V \kappa \nabla u \cdot \nabla T'(\vec{r},t) dV + \int_V u(Q_{laser} + Q_{NP}) dV$$

The term on the LHS takes into account time dependance, the first term on the RHS takes into account the boundary fluxes, the second term is the heat diffusion term, and the last term is the heat source. Inserting the expressions for $Q_{laser}$ and $Q_{NP}$ the heat source term becomes:

$$\int_V u(Q_{laser} \quad + \quad Q_{NP}) dV$$

$$\int_V u\mu_a \varphi(\vec{r},t) dV \quad + \quad \int_V u\sigma_a \sum_{i=1}^{N} \varphi(\vec{r},t)\delta(\vec{r} - \vec{r_i}) dV$$

$$\int_V u\mu_a \varphi(\vec{r},t) dV \quad + \quad u\sigma_a \sum_{i=1}^{N} \varphi(\vec{r_i},t)$$

This weak form of the heat diffusion equation can be used to solve for the temperature distribution using finite element methods. This form of the equation has decreased the order of the derivative of $T(\vec{r},t)$, which weakens the requirements of continuity of the variable. This simplifies the problem by getting rid of the singularity that comes with modeling each nanoparticle as a point heat source. It can be shown that if $T'(\vec{r},t)$ satisfies the weak form of the equation it is a good approximation of the solution to the strong form $T(\vec{r},t)$. The error in this approximation follows the form $|T(\vec{r},t) - T'(\vec{r},t)| \leq Ch^q$, where $C$ is a problem dependent constant, $h$ is the mesh spacing, and $q$ is a constant describing the order of convergence [7].
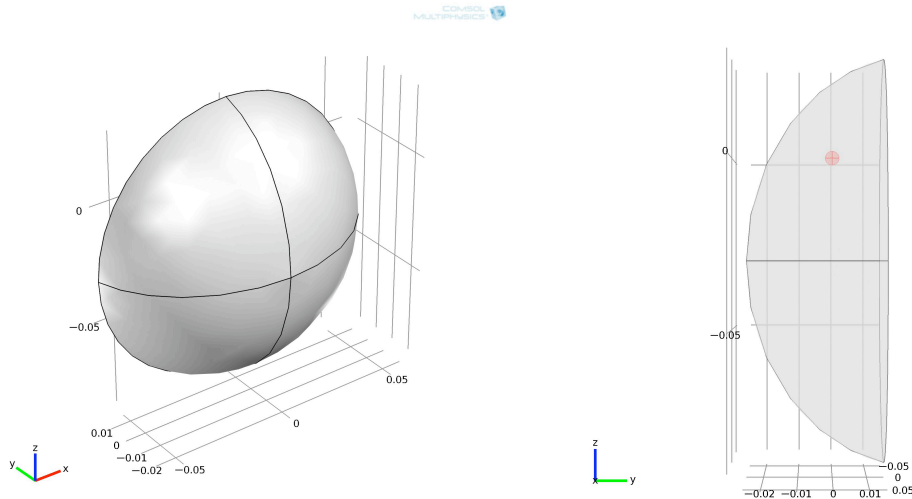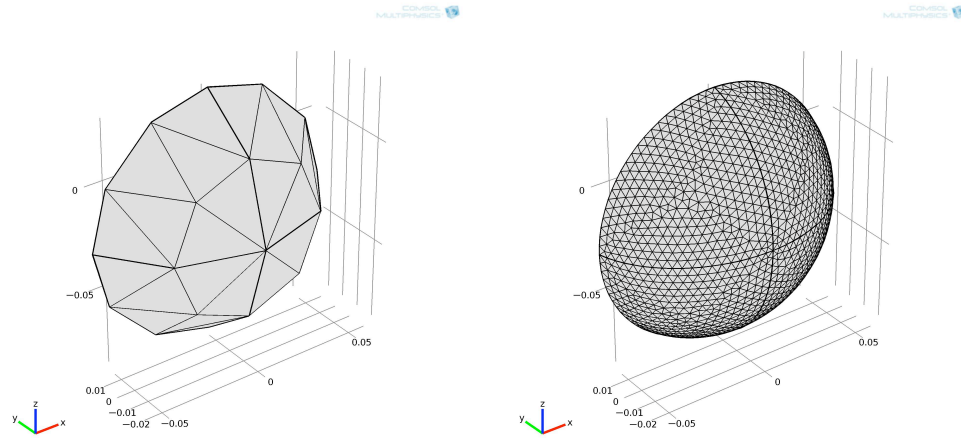
**Figure 9:** Breast phantom geometry as modeled in COMSOL. A full 3-dimensional model was used with the GNR-filled cavity shown in red.

## 4.2 FEM Model

Using the weak form of the heat diffusion equation, the breast phantom was modeled using the FEM software package COMSOL Multiphysics 4.1 (Comsol, Inc. , Burlington, MA.). The geometry of the phantom is shown in Figure 9 and was the exact geometry used for the linear superposition method. GNPs were modeled as uniformly distributed over the cavity and the number of GNPs was reduced using the same multiplication factor as in the linear superposition method. Figure 10 shows a close-up view of the cavity with an array of heat sources embedded within it. The number of particles was adjusted by increasing the size of the array, and only those particles inside the cavity acted as heat sources.
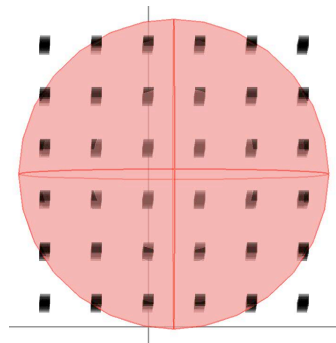


**Figure 10:** Breast phantom geometry as modeled in COMSOL. A close-up view at the cavity and the point heat sources uniformly distributed within the cavity.

20

**Figure 11:** Breast phantom geometry as modeled in COMSOL with different mesh size.
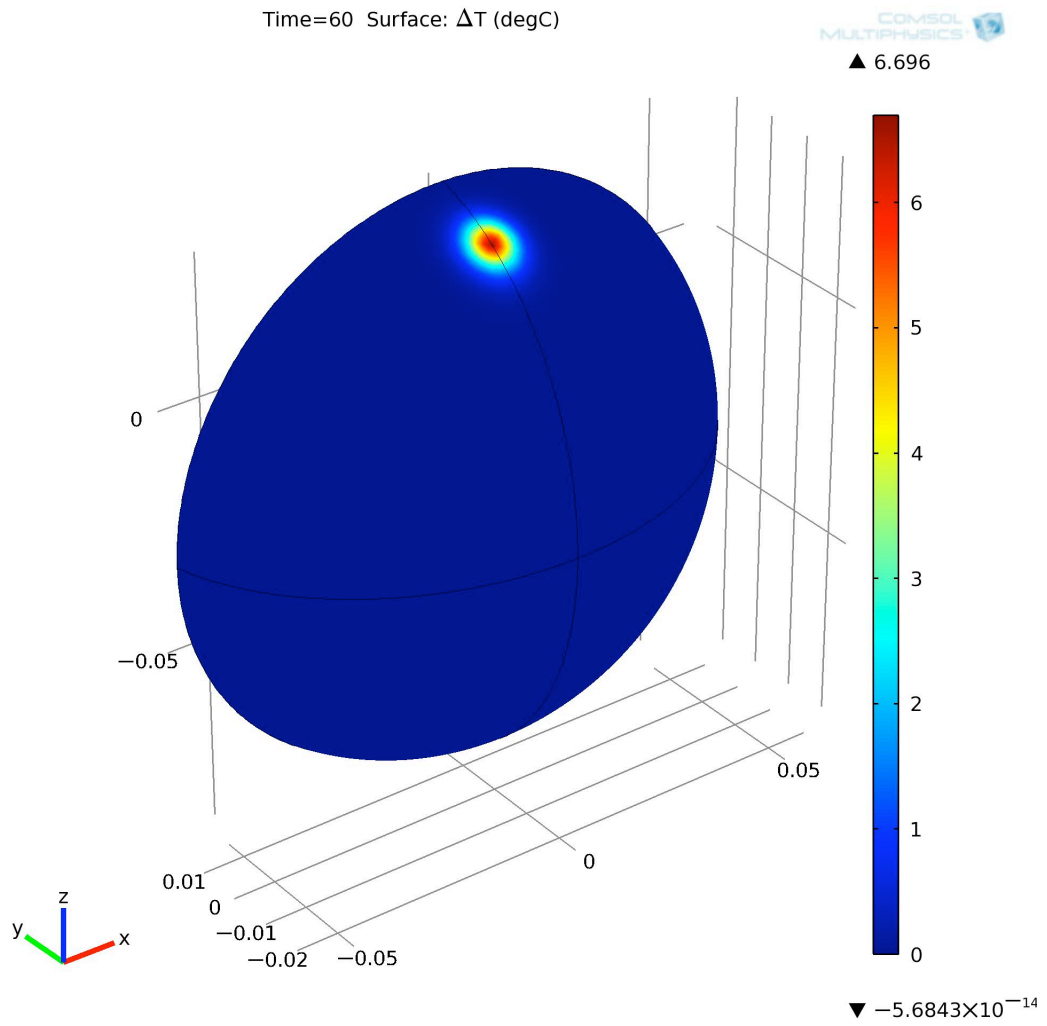
## 4.3 Results

The optical and thermal parameters were set the same as those used in the linear superposition model. The mesh size was chosen as fine as possible in order to reduce uncertainties in the solution. The default mesh sizes in COMSOL were used, these range from *extremely coarse* to *extremely fine*. Figure 11 shows the difference between an *extremely coarse* mesh and an *extra fine* mesh for the breast model used. Figure 12 shows the temperature profiles for different mesh sizes showing convergence to $< 1.3\%$ between the two finest mesh sizes used, *extra fine* and *finer*. The reduced number of GNPs was also varied and temperature profiles down the laser axis are shown on Figure 13 exhibiting convergence to $< 0.3\%$ for $np \geq 3053$. Surface temperatures can be visualized in 3D and presented in Figure 14, showing a maximum temperature increase of $6.7°$ C at the surface. The 2D temperature distribution is shown in Figure 15 and matches that of the linear superposition model. The temperature profile reflects this match much more clearly where it shows agreement to $\leq 1.2\%$ along the laser axis as shown in Figure 16.
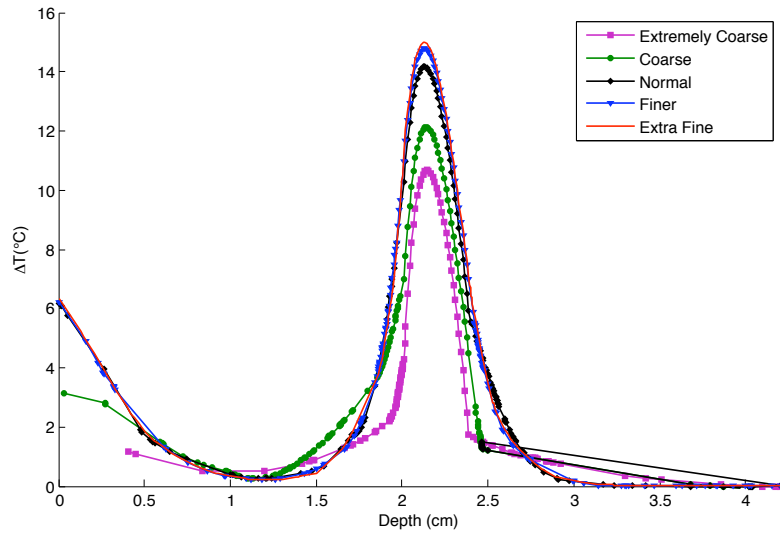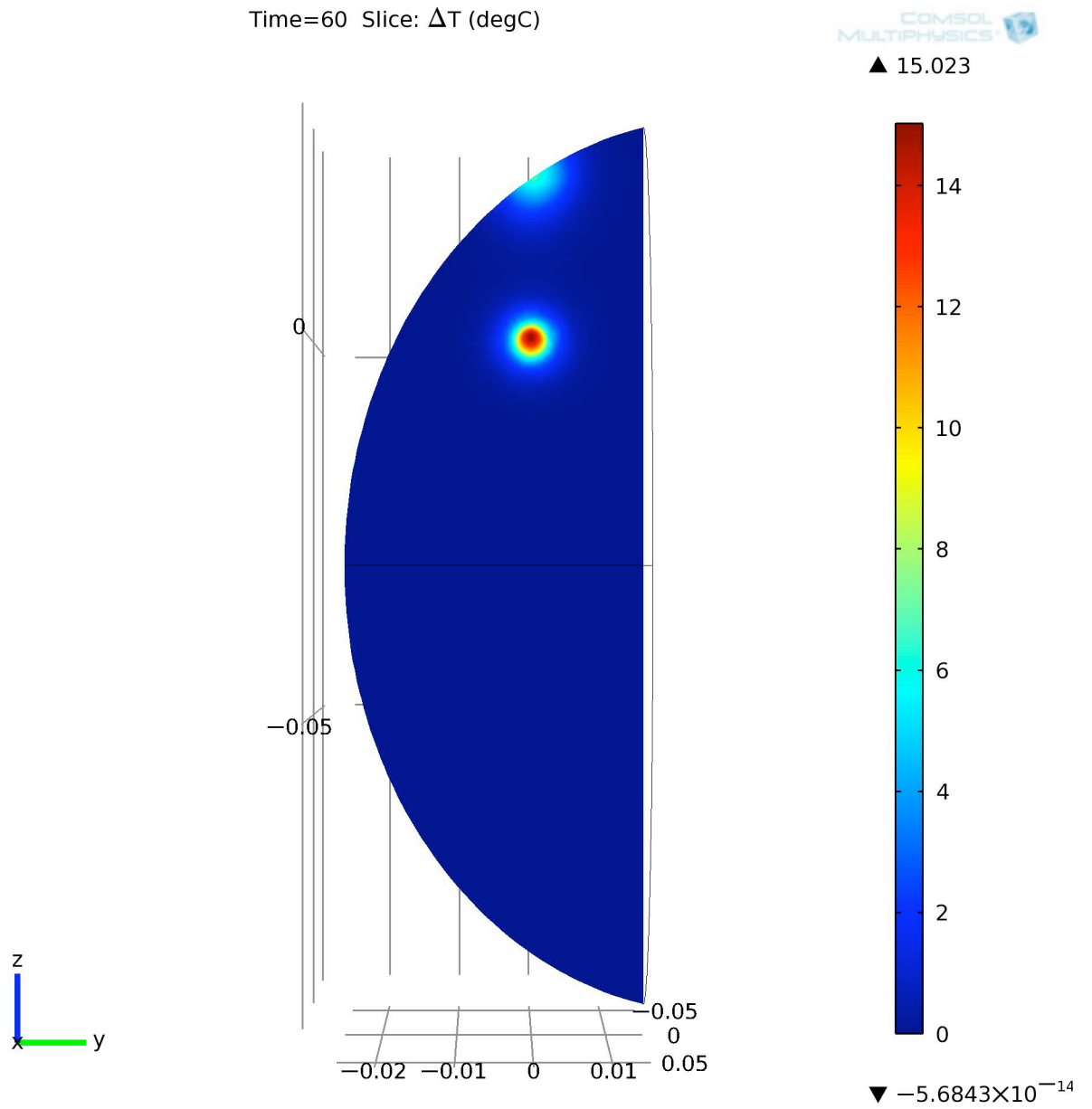
**Figure 12:** Temperature profile at t=1 min along the laser axis on the breast phantom. Curves are shown for different mesh sizes demonstrating convergence of the solution.
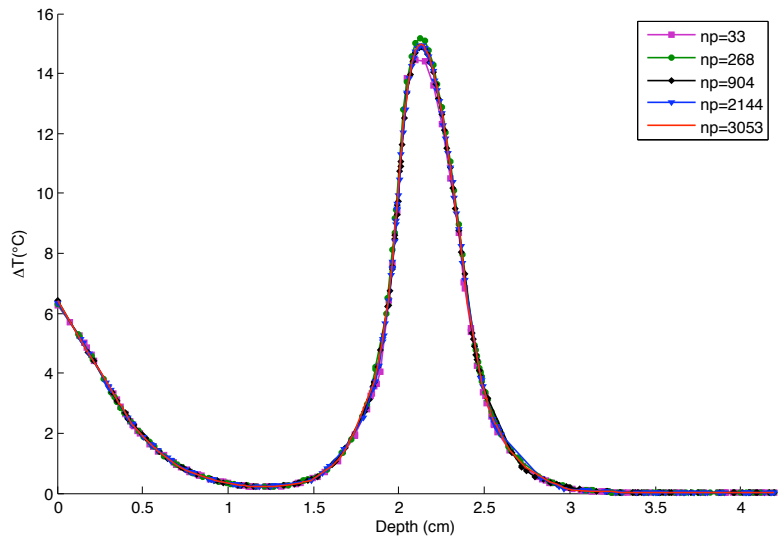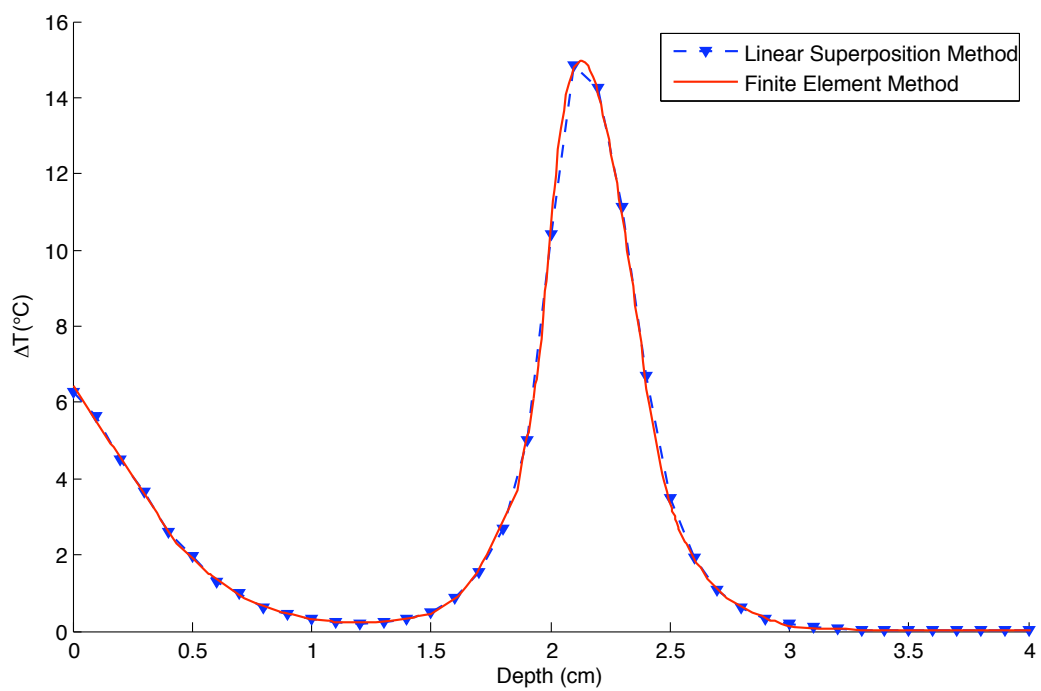


**Figure 13:** Temperature profile at t=1 min along the laser axis on the breast phantom. Curves are shown for different reduced number of nanoparticles $np$ demonstrating convergence of the solution.

**Figure 14:** 3D surface temperature distribution at t=1 min using the FEM.

**Figure 15:** 2D temperature distribution at t=1 min using the FEM.

**Figure 16:** Temperature profile at t=1 min along the laser axis on the breast phantom comparing the results from the linear superposition model and those of FEM.

# CHAPTER V

# CONCLUSION

The results from both models showed remarkable agreement, validating each other. The linear superposition model shows great flexibility as it is a pure superposition algorithm and allows any arbitrary GNP distribution. The FEM model has similar flexibility, but it's heavily limited by the choice in mesh size. This may pose a problem for situations in which high gradients of GNP concentration are present. This would create regions of high heat gradients, which would require very fine mesh sizes. The finest mesh size available to solve a specific problem can vary and is limited by computing power. An insufficiently fine mesh would lead to solutions that have not converged, and high uncertainty in the temperature distribution. On the other hand, the linear superposition model is not limited by such high GNP concentration gradients. This advantage comes at the cost of computation time, which is much longer than in the FEM model. This is mainly a result of the computation of the complementary error function $erfc(x)$, which can be approximated in order to improve computation time but at the cost of increased uncertainty.

The next step for both models is to test out how it predicts the heat distribution from an experimental phantom. This would require very good knowledge of the optical properties of the phantom material and full 3D temperature distribution. Both of these prerequisites demand a full experiment of their own. Scattering and absorption coefficients can be measured via spectroscopy techniques and full 3D temperature distribution can be measured via magnetic resonance thermometry. An experiment of that scale would test the ability of both techniques to accurately predict temperature distribution during GNP-mediated LITT. Experiments like these can also shed light into any practical issues that might arise from such a technique. Nevertheless, the success in developing the two computational techniques that validate each other, can be considered as a major step forward in the ability to develop a reliable treatment planning technique for GNP-mediated LITT.

# REFERENCES

[1] BOULNOIS, J.-L., "Photophysical processes in recent medical laser developments: a review," *Lasers in Medical Science*, vol. 1, pp. 47–66, August 1986.

[2] CARSLAW, H. S. and JAEGER, J. C., *Conduction of Heat in Solids.* 1993.

[3] CHEONG, S.-K., KRISHNAN, S., and CHO, S. H., "Modeling of plasmonic heating from individual gold nanoshells for near-infrared laser-induced thermal therapy," *Medical Physics*, vol. 36, pp. 4664–4671, October 2009.

[4] COX, B., "Introduction to laser-tissue interactions." Academic Website, October 2010.

[5] EL-SAYED, M. A., "Some interesting properties of metals confined in time and nanometer space of different shapes," *Accounts of Chemical Research*, vol. 34, no. 4, pp. 257–264, 2001.

[6] ELLIOT, A. M., STAFFORD, J., SCHWARTZ, J., WANG, J., SHETTY, A. M., BOURGOYNE, C., O'NEAL, P., and HAZLE, J. D., "Laser-induced thermal response and characterization of nanoparticles for cancer treatment using magnetic resonance thermal imaging," *Medical Physics*, vol. 34, pp. 3102–3108, July 2007.

[7] GOBBERT, M. K. and YANG, S., "Numerical demonstration of finite element convergence for lagrange elements in comsol multiphysics," in *Proceedings of the COMSOL Conference 2008 Boston*, 2008.

[8] HALL, E. J. and GIACCIA, A. J., *Radiobiology for the Radiologist.* Lippincott Williams and Williams, sixth ed., 2006.

[9] HEUSMANN, H., KÖLZER, J., and MITIC, G., "Characterization of female breasts invivo by time resolved and spectroscopic measurements in near infrared spectroscopy," *Journal of Biomedical Optics*, vol. 1, pp. 425–434, October 1996.

[10] IIZUKA, M. N., VITKIN, I. A., KOLIOS, M. C., and SHERAR, M. D., "The effects of dynamic optical properties during intersittial laser photocoagulation.," *Physics in Medicine and Biology*, vol. 45, pp. 1335–1357, 2000.

[11] JAIN, P. K., HUANG, X., EL-SAYED, I. H., and EL-SAYED, M. A., "Review of some interesting surface plasmon resonance-enhanced properties of noble metal nanoparticels and their application to biosystems," *Plasmonics*, vol. 2, pp. 107–118, 2007.

[12] KELLY, K. L., CORONADO, E., ZHAO, L. L., and SCHATZ, G. C., "The optical properties of metal nanoparticles: The influence of size, shape, and dielectric environment," *The Journal of Physical Chemistry B*, vol. 107, pp. 668–677, 2003.

[13] MAEDA, H., "Tumor vascular permeability and the epr effect in macromolecular therapeutics: a review," *Journal of Controlled Release*, vol. 65, pp. 271–284, 2000.

[14] McKenzie, A. L., "Physics of thermal processes in laser-tissue interactions," *Physics in Medicine and Biology*, vol. 35, pp. 1175–1209, March 1990.

[15] Niemz, M. H., *Laser-Tissue Interactions: Fundamentals and Application.* Springer, third ed., 2007.

[16] Nyborg, W. L., "Solutions of the bio-heat transfer equation," *Physics in Medicine and Biology*, vol. 33, no. 7, pp. 785–792, 1988.

[17] Rao, S. S., *The Finite Element Method in Engineering.* Elsevier Inc., fifth ed., 2011.

[18] van der Zee, J., "Heating the patient: a promising approach?," *Annals of Oncology*, vol. 13, pp. 1173–1184, 2002.